Supporting Information

Novel 3D Cubic Topology in Hybrid Lead Halides with a Symmetric Aromatic Triammonium Exhibiting Water Stability

Eugenia S. Vasileiadou, [1] Imra S. Tajuddin, [1] Michael C. De Siena, [1] Vladislav V. Klepov, [1] Mikaël Kepenekian, [2] George Volonakis, [2] Jacky Even, [3] Lukasz Wojtas, [4] Ioannis Spanopoulos, [4] Xiuquan Zhou, [5] Abishek K. Iyer, [1] Julie L. Fenton, [1] William R. Dichtel, [1] and Mercouri G. Kanatzidis [1,*]

[1] *Department of Chemistry, Northwestern University, Evanston, IL 60208, United States.*

[2] *Univ Rennes, ENSCR, CNRS, ISCR − UMR 6226, F-35000 Rennes, France.*

[3] *Univ Rennes, INSA Rennes, CNRS, Institut FOTON − UMR 6082, F-35000 Rennes, France*

[4] *Department of Chemistry, University of South Florida, Tampa, Florida 33620, United States*

[5] *Materials Science Division, Argonne National Laboratory, Lemont, Illinois 60439, USA*

Table of Contents

1. Methods

XRD Measurements:

Single-crystal X-ray diffraction

Single crystal diffraction experiments were performed using a four-circle Rigaku XtaLAB Synergy system equipped with a PhotonJet (Mo, λ= 0.71073 Å) micro-focus sealed X-ray tube. Intensity data of single crystals were collected at 293 K. Suitable single crystals were mounted on a glass fiber with grease on an XtaLAB Synergy diffractometer equipped with a (micro-focus sealed X-ray tube PhotonJet (Mo) X-ray source and a Hybrid Pixel Array Detector (HyPix) detector. Temperature of the crystal was controlled with an Oxford Cryosystems low-temperature device. Data reduction was performed with the CrysAlisPro software using an empirical absorption correction. The structure was solved with the ShelXT structure solution program using the direct methods solution method and by using Olex2 as the graphical interface.[1-2] The model was refined with ShelXL using least squares minimization.[2-3] Crystals of $T_7Pb_3Br_{27}$·DMF and $T_2Sn_3Br_{18}$·$4H_2O$·$0.5Br_2$ did not diffract past ca. 1.1 Å resolution. Due to heavy disorder, it was impossible to reliably identify cations / solvent in the structural cavity. Olex2 Solvent mask was used to account for disordered content.

Powder X-ray diffraction

Powder X-ray diffraction patterns were collected on a Rigaku Miniflex system (CuKα radiation) operated at 40 kV and 15 mA. A typical scan rate was 15 sec/step with a step size of 0.02 deg.

Thermal Analysis:

Differential scanning calorimetry (DSC) measurements were performed on a Netzsch's Simultaneous Thermal Analysis (STA) system. An amount of ~10 mg of sample was placed inside an alumina cap and DSC measurements were performed at a scan rate of 5 °C/min in sealed aluminum pans under He (211.0 mL/min).

Optical Absorption Spectroscopy:

Optical diffuse reflectance measurements were performed using a Shimadzu UV-3600 UV−VIS NIR spectrometer operating in the 200−2500 nm region at room temperature. $BaSO_4$ was used as a non-absorbing reflectance reference for all measurements. The bandgap was estimated by diffuse reflectance spectroscopy on powder samples of the studied materials, where the Kubelka-Munk model was used to derive absorption values.[4]

Steady-State and Time-Resolved Photoluminescence:

PL spectra were collected using an Edinburgh Instruments FS5 spectrofluorometer. A 150 W Xe lamp was used to collect steady-state spectra and a 375 nm pulsed diode laser was used to collect time-resolved spectra. 78 K spectra were collected using a liquid nitrogen finger dewar coupled to the spectrofluorometer.

Electronic Structure Calculations:

First-principles calculations are based on density functional theory (DFT) as implemented in the SIESTA package.[5-6] The nonlocal van der Waals density functional of Dion *et al.* corrected by Cooper (C09) is used for geometry optimizations.[7-8] Spin-orbit coupling is taken into account through the so-called off-site approach as following the Hemstreet formalism.[9] To prevent conflicts between the treatment of spin-orbit coupling and the nonlocality of C09, single point calculations are conducted with the revPBE functional on which C09 is based.[10] Core electrons are described with Troullier-Martins pseudopotentials [11], while valence wavefunctions are developed over double-ζ polarized basis set of finite-range numerical pseudoatomic orbitals.[12] In all cases, an energy cutoff of 150 Ry for real-space mesh size has been used. Experimental structures are used for the inorganic skeleton, well characterized by X-ray diffraction. As this is not the case for light atoms, the positions of organic cations have been optimized. Crystal orbital Hamilton population (COHP) analysis is performed using the scheme available in SIESTA.[13]

Nuclear Magnetic Resonance:

^{1}H and ^{13}C NMR spectra were recorded on 600 MHz Bruker, A600 spectrometer.

Microscope Images:

Nikon SMZ1500 microscope was used for visualization of crystal samples and acquisition of high-resolution images

2. Characterization

2.1 Single Crystal X-ray Diffraction

Table S1. Crystal Data and Structure Refinement for $T_7Pb_3Br_{27}$·DMF and $T_4Sn_3Br_{24}$.

	$T_7Pb_3Br_{27}$·DMF	$T_2Sn_3Br_{18}$·$4H_2O$·$0.5Br_2$
Empirical formula	$C_{171}H_{175}N_{22}OPb_3Br_{27}$	$C_{48}H_{56}N_6OSn_3Br_{18.5}$
Crystal system	trigonal	monoclinic
Space group	*R*-3*c*	$P2_1/n$
Crystal Shape	Clear Needle	Light Yellow Needle
Unit cell dimensions (Å)	a = b =29.014(2) Å, c= 34.682(4) Å γ = 120°	a = 17.436(15) Å, b = 7.362(6) Å, c = 30.01(3) Å, β = 94.163(10)°
Volume ($Å^3$)	25284(5)	3842(6)
Z	6	2
Density (calculated, g/cm^3)	1.793	2.202
Independent reflections	2217 [R_{int} = 0.1271]	1742 [R_{int} = 0.2127]
Completeness to θ = 18.847°/ 15.776°	99.6%	96.3%
Data / restraints / parameters	2217 / 169 / 255	1742 / 7 / 217
Goodness-of-fit	1.051	1.171
Final R indices [I>3σ(I)]	R_{obs} = 0.0557, wR_{obs} = 0.1458	R_{obs} = 0.0930, wR_{obs} = 0.2458
R indices [all data]	R_{all} = 0.0839, wR_{all} = 0.1578	R_{all} = 0.1357, wR_{all} = 0.3117

$R = \Sigma||Fo|-|Fc|| / \Sigma|Fo|$, $wR = \{\Sigma[w(|Fo|2 - |Fc|2)2] / \Sigma[w(|Fo|4)]\}1/2$ and $w=1/(\sigma2(I)+0.0004I2)$

2.2 Powder X-ray Diffraction Measurements

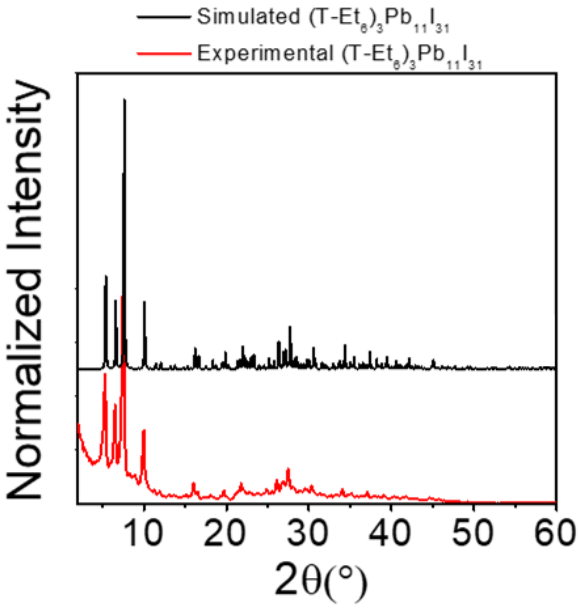

Figure S1. Comparison of the experimental PXRD pattern from crystals with the simulated PXRD pattern from the solved single crystal structure of $(T\text{-}Et_6)_3Pb_{11}I_{31}$.

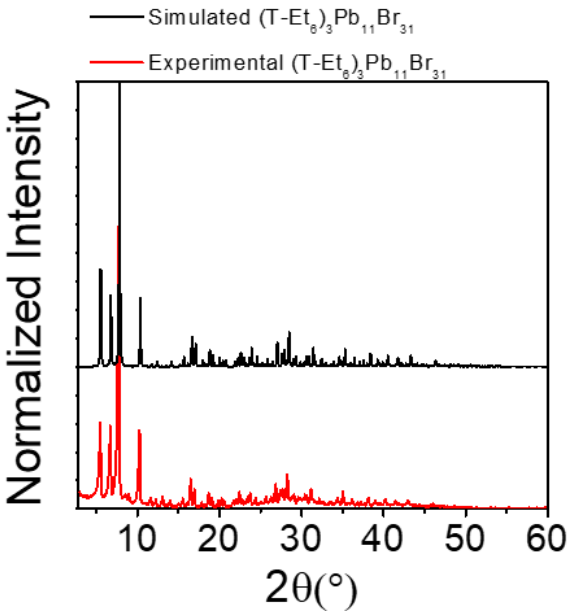

Figure S2. Comparison of the experimental PXRD pattern from crystals with the simulated PXRD pattern from the solved single crystal structure of $(T\text{-}Et_6)_3Pb_{11}Br_{31}$.

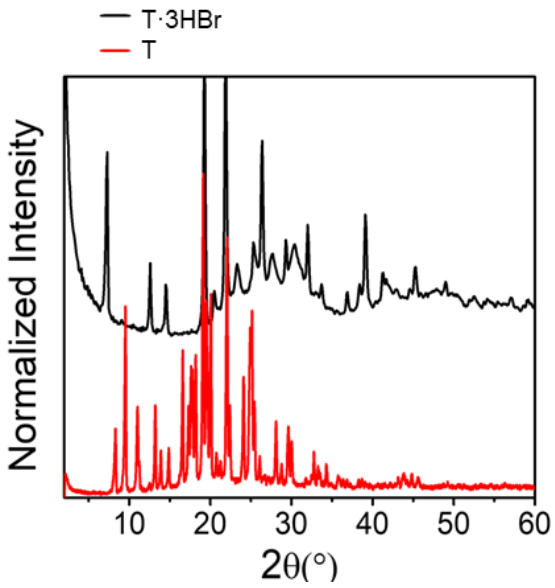

Figure S3. Comparison of the experimental PXRD pattern from crystals of 1,3,5-Tris(4-aminophenyl)benzene (T) with the experimentally observed PXRD pattern from its protonated verison T·3HBr demonstrating structural variation between the two species.

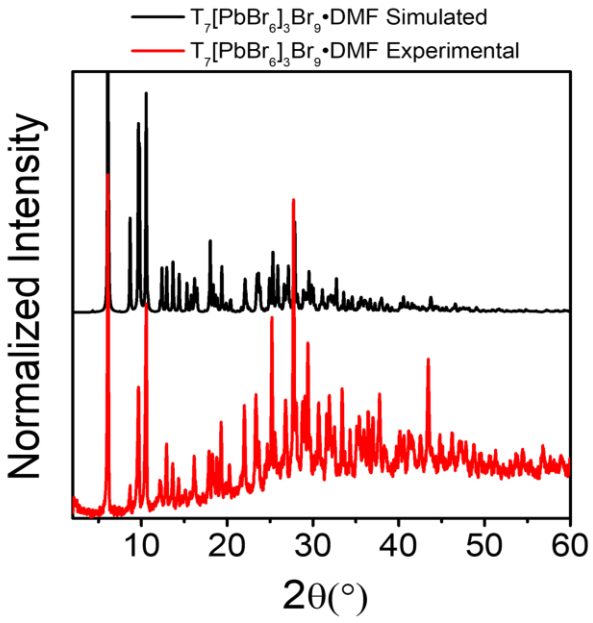

Figure S4. Comparison of the experimental PXRD pattern from crystals with the simulated PXRD pattern from the solved single crystal structure of $T_7[PbBr_6]_3Br_9$•DMF.

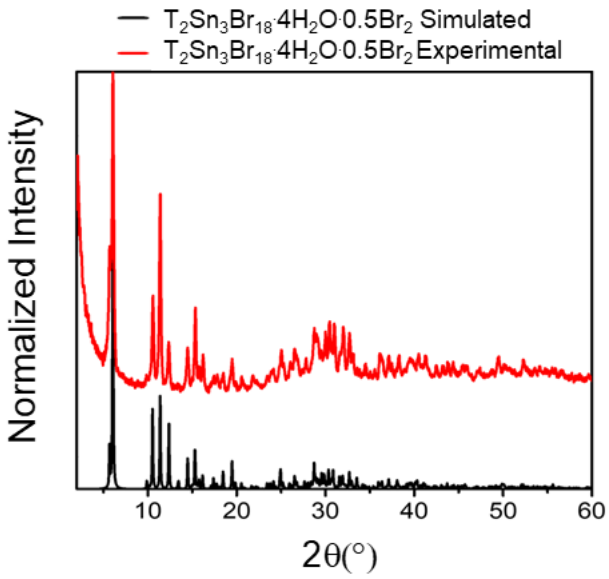

Figure S5. Comparison of the experimental PXRD pattern from crystals with the simulated PXRD pattern from the solved single crystal structure of $T_2Sn_3Br_{18}·4H_2O·0.5Br_2$.

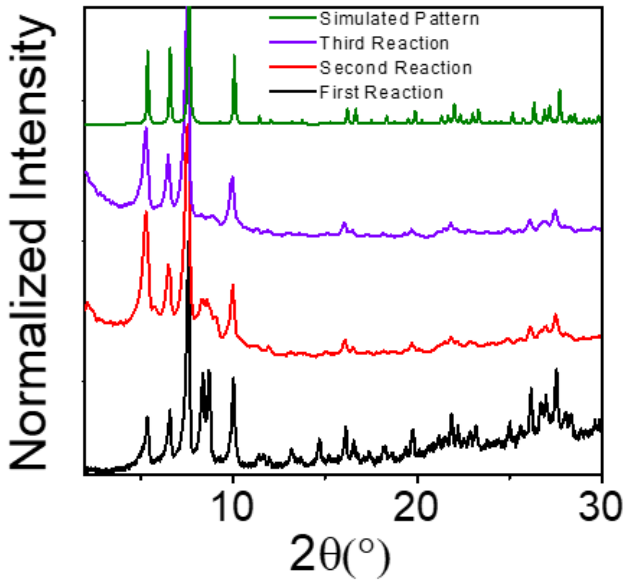

Figure S6. Comparison of the experimental PXRD patterns of three separate synthetic repetitions of (T-Et6)3Pb11I31 in identical conditions, along with the simulated PXRD that confirm the reproducibility of the synthesis.

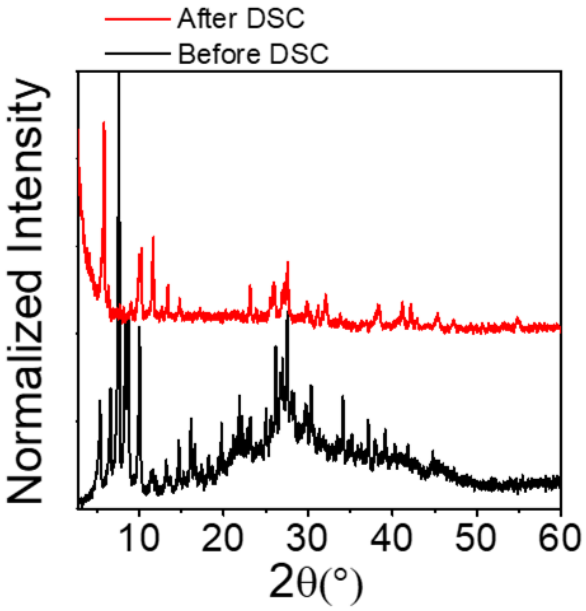

Figure S7. Comparison of the experimental PXRD pattern of $(T\text{-}Et_6)_3Pb_{11}I_{31}$ before and after DSC scan.

2.3 Thermal analysis

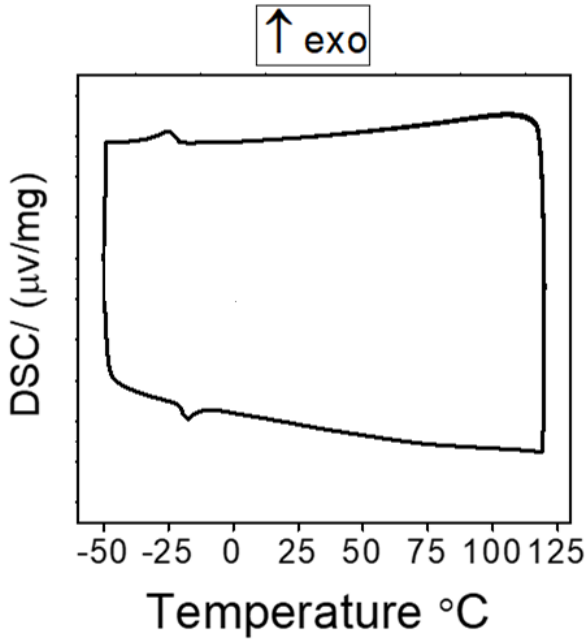

Figure S8. Thermal behavior of $(T\text{-}Et_6)_3Pb_{11}I_{31}$ **(A)** DSC scan from -50°C to 120°.

2.4 Photoluminescence Spectroscopy and Optical Properties

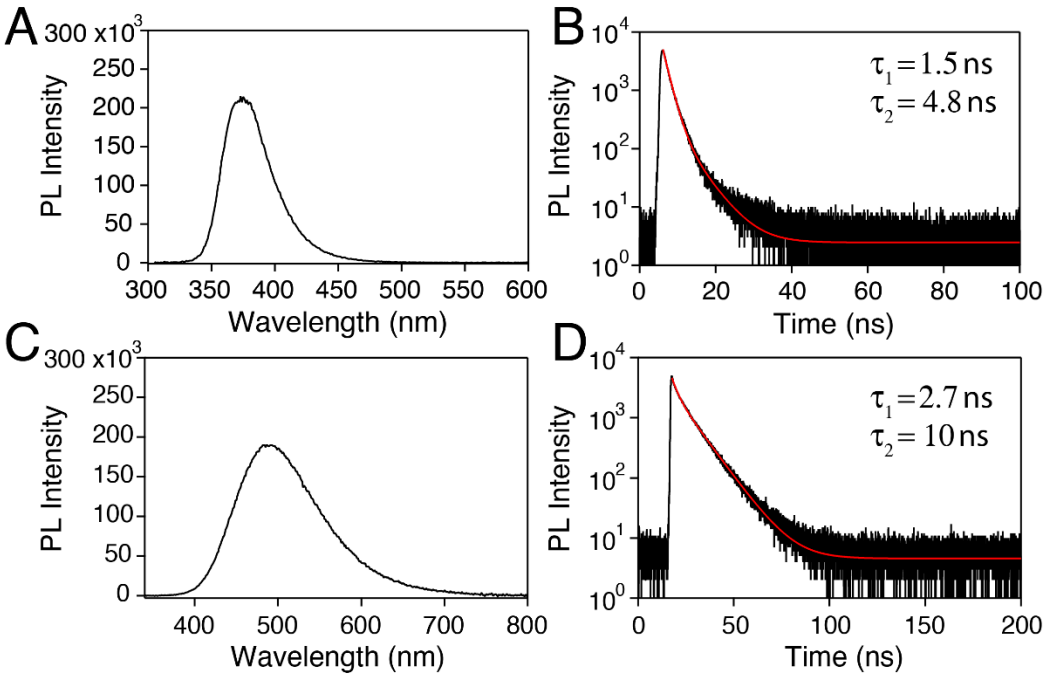

Figure S9. Steady-state **(A)** and time-resolved **(B)** spectra for the pure triamine compound, T, taken in solution (dissolved in toluene). This species exhibits UV emission with fast biexponential decay dynamics. Solution steady-state **(C)** and time-resolved **(D)** spectra for the pure T·3HBr compound (dissolved in methanol). This compound displays broad white-light emission centered at 500 nm with biexponential decay dynamics.

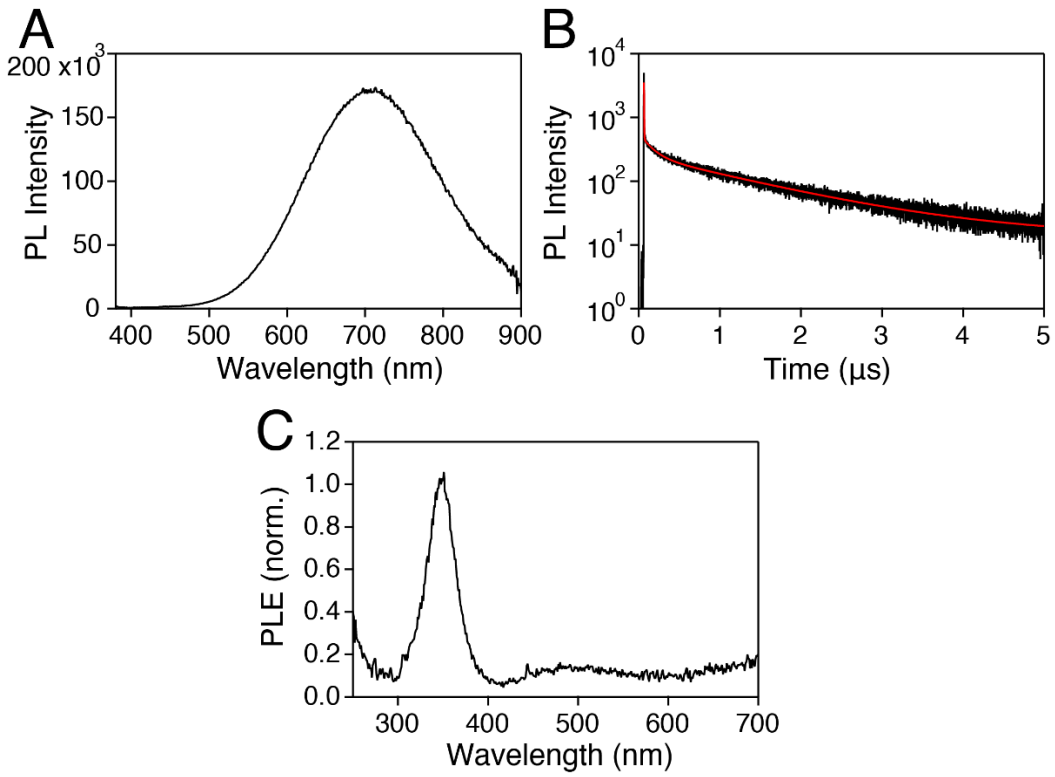

Figure S10. (A) Steady-state PL emission spectrum for $T_2Sn_3Br_{18}{\cdot}4H_2O{\cdot}0.5Br_2$ when excited at 355 nm. The compound displays broad emission centered at 710 nm with a FWHM of 200 nm. This feature is assigned to self-trapped excitonic emission. **(B)** Time-resolved PL emission spectrum for $T_2Sn_3Br_{18}$ showing long recombination dynamics. The decay is fitted to a triexponential with lifetimes of 2.2 ns, 138 ns, and 1.4 µs with an average decay of 1.2 µs. **(C)** gives the photoluminescence excitation spectrum for the compound monitoring the emission at 710 nm. We assign the strong band centered at 350 nm to electronic transitions in isolated $[SnBr_6]^{4-}$ octahedra.

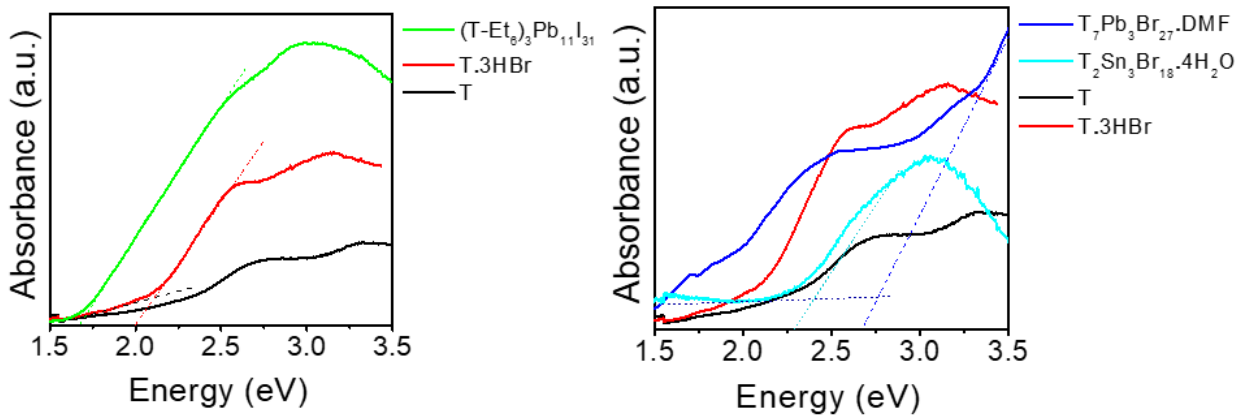

Figure S11. UV−vis absorption spectra of studied compounds at room temperature; the dashed lines indicate the energy of the absorption onset.

2.5 Electronic Calculations

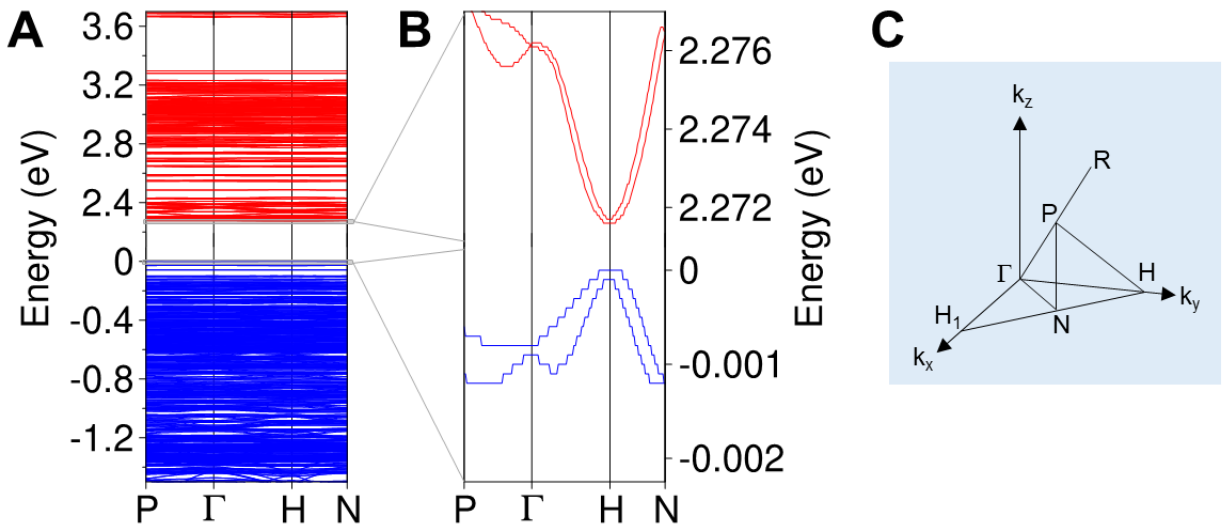

Figure S12. (A) DFT computed band structure of $(T\text{-}Et_6)_3Pb_{11}I_{31}$. **(B)** Same close to band edges. Very weak dispersions are obtained in all directions of the Brillouin zone. **(C)** Brillouin zone of Ia-3.

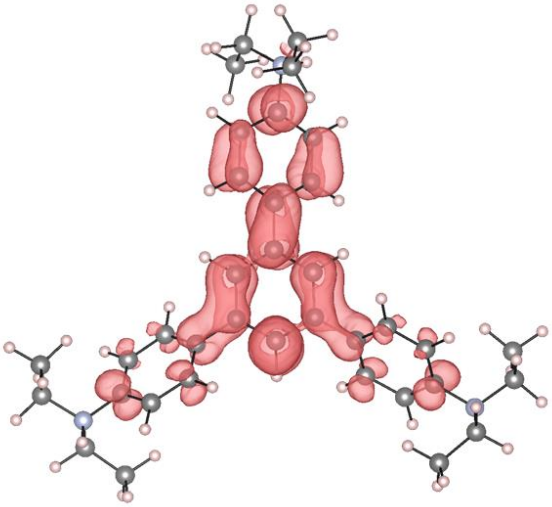

Figure S13. Partial charge densities taken at the conduction band minimum (CBM, red) of (T-Et_6)$_3$$Pb_{11}I_{31}$, showing only the contribution of one T-Et_6 organic cation.

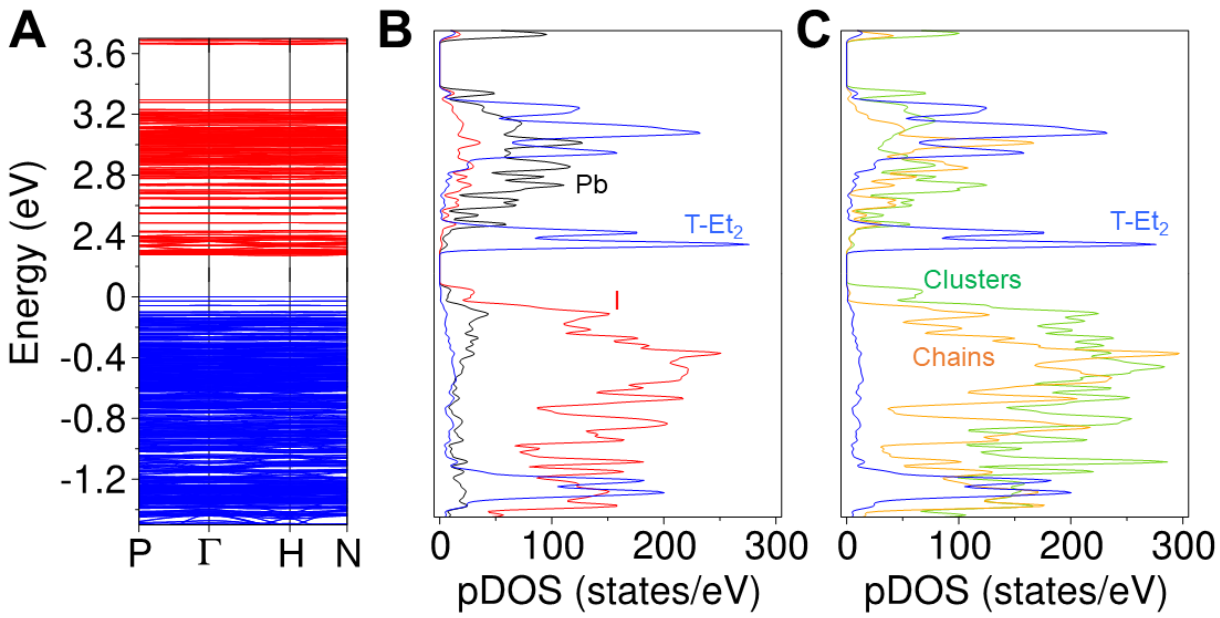

Figure S14. (A) DFT computed band structure of (T-Et_6)$_3$$Pb_{11}I_{31}$. **(B)** Density of states projected over Pb (black), I (red) and T-Et_6 (blue) states. **(C)** Same projected over T-Et_6 (blue), the 5 face-sharing octahedra chain (orange) and the 6 edge-sharing octahedra cluster (green).

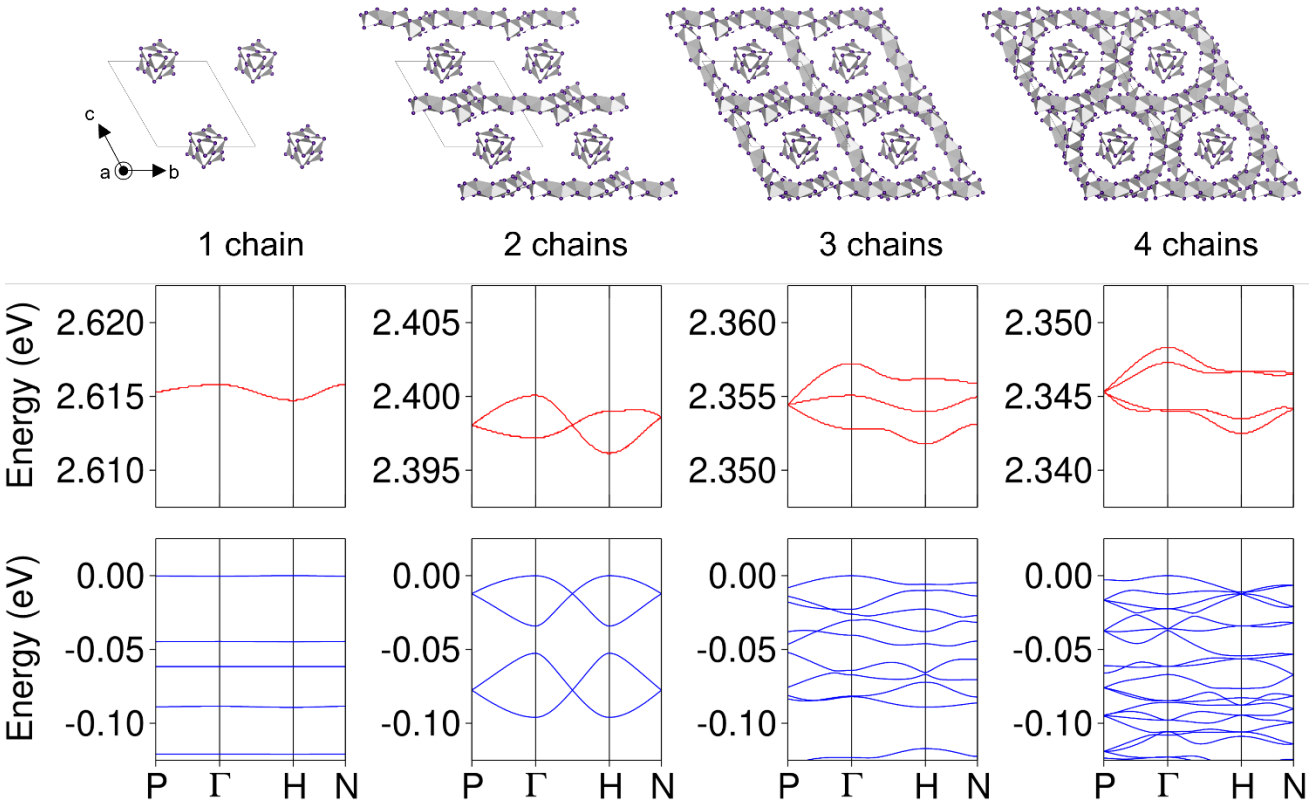

Figure S15. DFT computed band structure of $(T\text{-}Et_6)_3Pb_{11}I_{31}$ considering 1 to 4 (all) chains. Organic cations are emulated by a background charge.

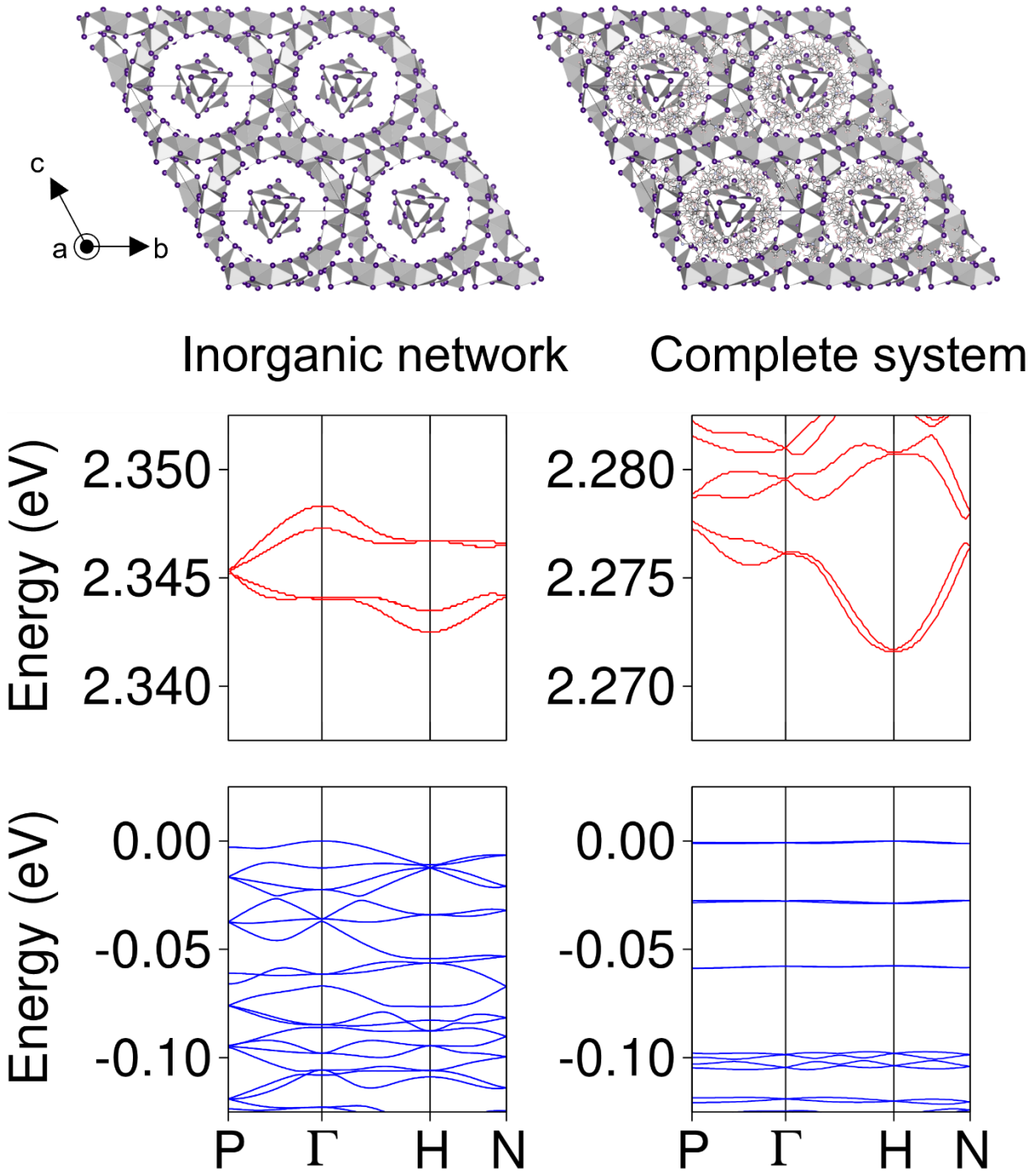

Figure S16. DFT computed band structure of $(T\text{-}Et_6)_3Pb_{11}I_{31}$ considering (left) the inorganic network, while organic cations are emulated by a background charge, and (right) the complete system.

2.6 NMR Spectroscopy

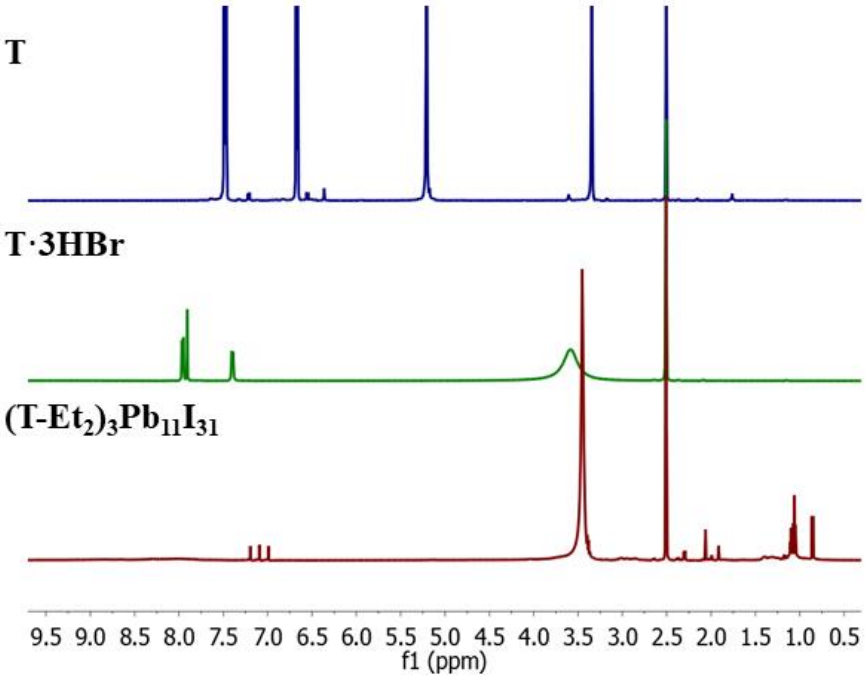

Figure S17. Proton NMR of 1,3,5-Tris(4-aminophenyl)benzene (T), ethylated T, and protonated T products.

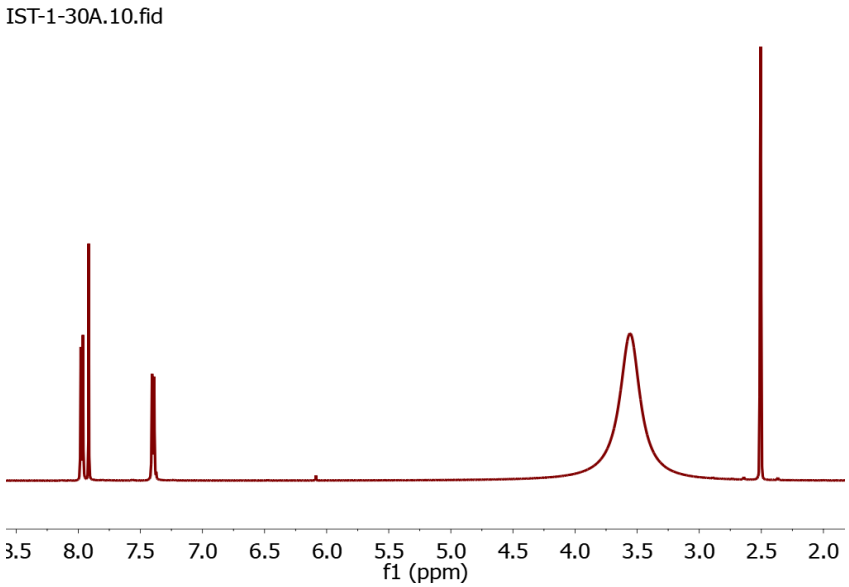

Figure S18. Proton NMR of $T_7[PbBr_6]_3Br_9$•DMF.

2.7 Microscope Images

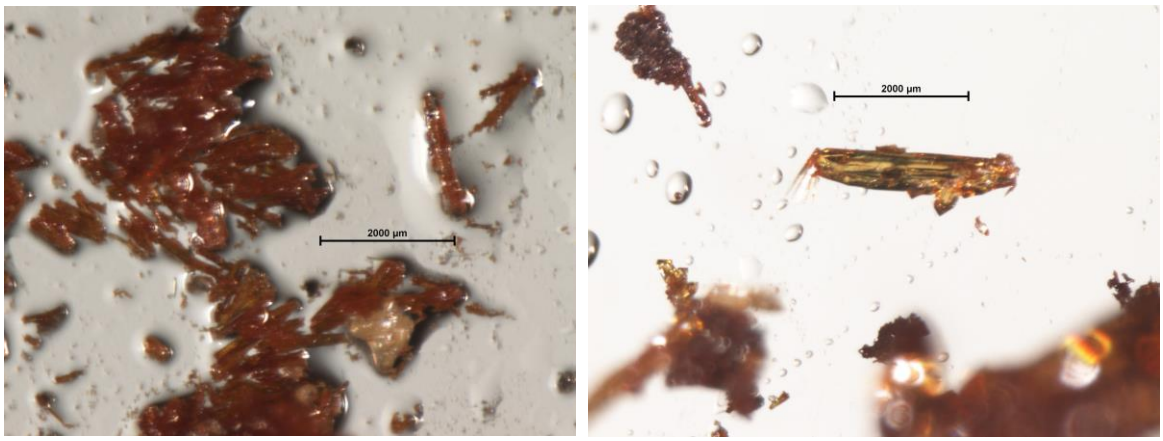

Figure S19. Microscope images of **(A)** fresh $(T\text{-}Et_6)_3Pb_{11}I_{31}$ crystals and **(B)** $(T\text{-}Et_6)_3Pb_{11}I_{31}$ crystals after 3 months.

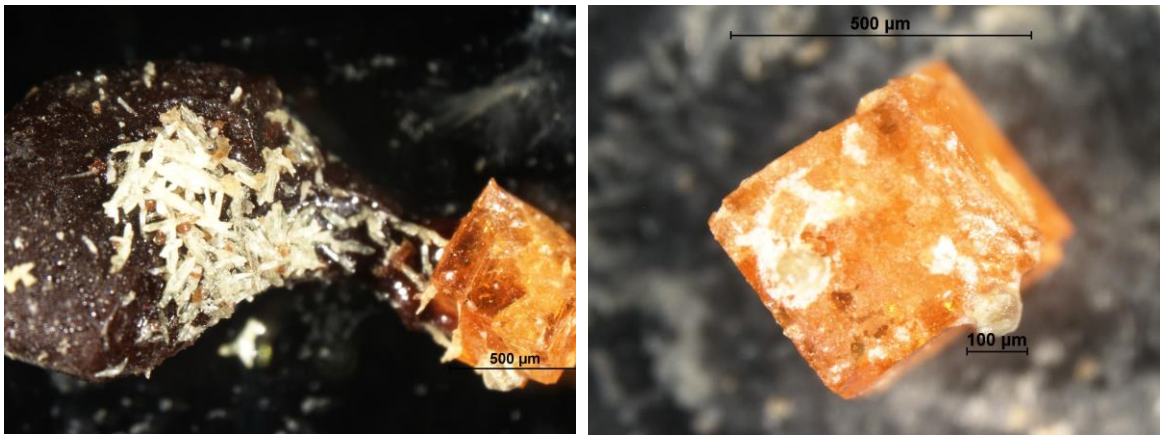

Figure S20. Microscope images of $(T\text{-}Et_6)_3Pb_{11}Br_{31}$ orange crystals along with yellow crystal byproduct.

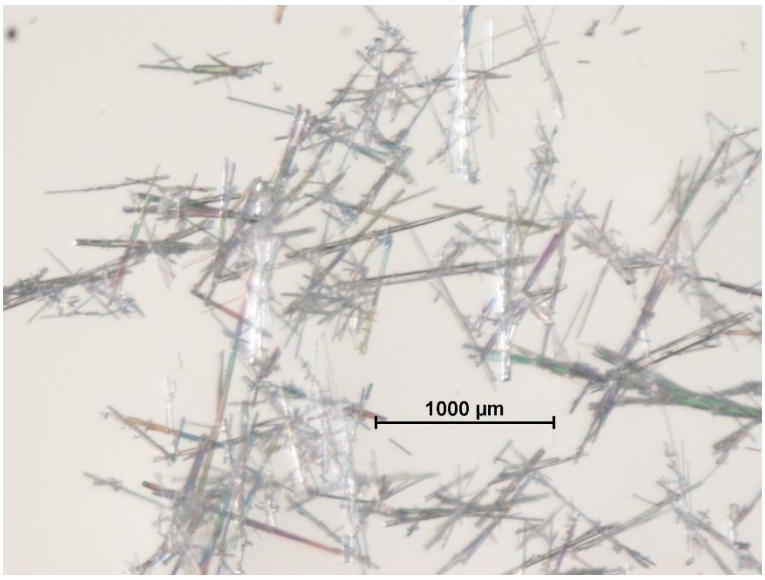

Figure S21. Microscope image of $T_7[PbBr_6]_3Br_9$•DMF crystals.

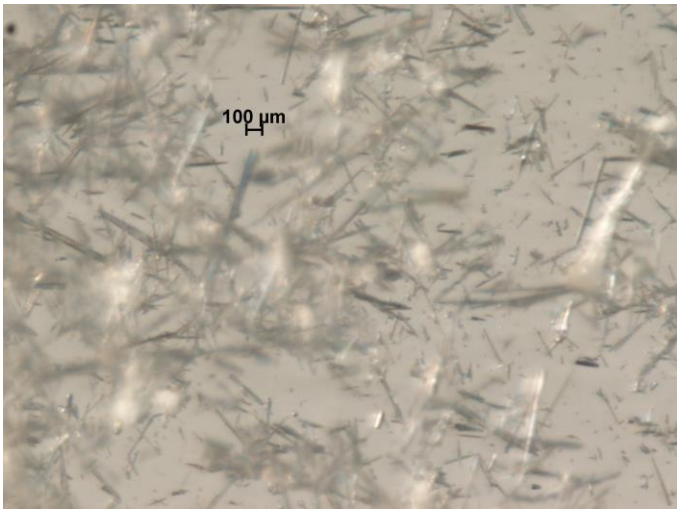

Figure S22. Microscope image of $T_2Sn_3Br_{18}·4H_2O·0.5Br_2$ crystals.

2.8 Crystallographic Tables

Table S2. Pb-I bond distances (Å) and Pb-I-Pb angles (º) for $(T\text{-}Et_6)_3Pb_{11}I_{31}$.

Label	Distances	Label	Angles (°)
Pb(2)-I(006)#1	3.180(3)	Pb(2)-I(006)-Pb(2)#7	99.96(9)
Pb(2)-I(006)	3.063(6)	Pb(2)-I(006)-Pb(1)	1.61(14)
Pb(2)-I(3)#2	3.430(8)	Pb(2)#7-I(006)-Pb(1)	98.42(7)
Pb(2)-I(3)	3.218(7)	Pb(2)-I(006)-Pb(1)#7	100.07(6)
Pb(2)-I(1)	3.002(3)	Pb(2)#7-I(006)-Pb(1)#7	6.21(16)
Pb(2)-I(2)	2.952(3)	Pb(1)#7-I(006)-Pb(1)	98.60(18)
Pb(2)-I(0AA)#2	3.291(16)	Pb(2)-I(3)-Pb(2)#6	98.62(13)
Pb(02)-I(008)#3	3.2190(8)	Pb(2)-I(3)-Pb(04)	100.54(15)
Pb(02)-I(008)	3.2191(8)	Pb(04)-I(3)-Pb(2)#6	96.38(17)
Pb(02)-I(008)#4	3.2190(8)	Pb(1)-I(3)-Pb(2)	6.01(17)
Pb(02)-I(008)#5	3.2190(8)	Pb(1)#6-I(3)-Pb(2)	98.47(12)
Pb(02)-I(008)#6	3.2190(8)	Pb(1)-I(3)-Pb(2)#6	98.22(11)
Pb(02)-I(008)#2	3.2190(8)	Pb(1)#6-I(3)-Pb(2)#6	1.51(17)
Pb(03)-I(008)#2	3.2534(10)	Pb(1)-I(3)-Pb(04)	94.6(3)
Pb(03)-I(008)#6	3.2534(10)	Pb(1)#6-I(3)-Pb(04)	94.9(2)
Pb(03)-I(008)	3.2533(10)	Pb(1)#6-I(3)-Pb(1)	97.9(2)
Pb(03)-I(009)#6	3.2063(11)	Pb(02)-I(008)-Pb(03)	77.38(2)
Pb(03)-I(009)	3.2062(11)	Pb(04)-I(009)-Pb(03)	80.24(3)
Pb(03)-I(009)#2	3.2063(11)	Pb(2)-I(1)-Pb(1)	5.93(15)
Pb(04)-I(3)#2	3.399(6)		
Pb(04)-I(3)	3.399(6)		
Pb(04)-I(3)#6	3.399(6)		
Pb(04)-I(009)#6	3.1209(11)		

Pb(04)-I(009)#2	3.1209(11)
Pb(04)-I(009)	3.1209(11)
Pb(04)-I(0AA)#6	3.251(15)
Pb(04)-I(0AA)	3.251(15)
Pb(04)-I(0AA)#2	3.251(15)

Table S3. Pb-Br bond distances (Å) and Pb-Br-Pb angles (º) for $(T\text{-}Et_6)_3Pb_{11}Br_{31}$.

Label	**Distances**	**Label**	**Angles (°)**
Pb(1)-Br(1)#1	3.008(2)	Pb(1)-Br(1)-Pb(1)#8	101.20(6)
Pb(1)-Br(1)	2.962(2)	Br(3)-Br(2)-Pb(1)	78.0(4)
Pb(1)-Br(2)	2.882(4)	Br(2)-Br(3)-Pb(1)	83.1(4)
Pb(1)-Br(3)	2.839(4)	Pb(1)#3-Br(4)-Pb(1)	96.26(6)
Pb(1)-Br(4)#2	3.134(2)	Pb(1)-Br(4)-Pb(2)	98.15(6)
Pb(1)-Br(4)	3.154(2)	Pb(1)#3-Br(4)-Pb(2)	98.55(7)
Pb(2)-Br(4)#3	3.229(3)	Pb(2)-Br(5)-Pb(3)	81.84(6)
Pb(2)-Br(4)#2	3.229(3)	Pb(4)-Br(6)-Pb(3)	79.09(5)
Pb(2)-Br(4)	3.229(3)		
Pb(2)-Br(5)	2.983(3)		
Pb(2)-Br(5)#3	2.983(3)		
Pb(2)-Br(5)#2	2.983(3)		
Pb(3)-Br(5)	3.083(3)		
Pb(3)-Br(5)#3	3.083(3)		
Pb(3)-Br(5)#2	3.083(3)		
Pb(3)-Br(6)	3.143(3)		
Pb(3)-Br(6)#3	3.143(3)		
Pb(3)-Br(6)#2	3.143(3)		

Pb(4)-Br(6)#4	3.117(2)
Pb(4)-Br(6)#3	3.117(2)
Pb(4)-Br(6)#2	3.117(2)
Pb(4)-Br(6)	3.117(2)
Pb(4)-Br(6)#5	3.117(2)
Pb(4)-Br(6)#6	3.117(2)

Table S5. Pb-Br bond distances (Å) and Pb-Br-Pb angles (º) for $T_7Pb_3Br_{27}$·DMF.

Label	Distances	Label	Angles (°)
Pb(1)-Br(2)	2.911(3)	Br(2)#1-Pb(1)-Br(4)#1	171.55(10)
Pb(1)-Br(2)#1	2.910(3)	Br(2)-Pb(1)-Br(4)	171.56(10)
Pb(1)-Br(3)	2.962(2)	Br(3)#1-Pb(1)-Br(3)	175.48(13)
Pb(1)-Br(3)#1	2.962(2)	Br(4)#1-Pb(1)-Br(4)	105.22(14)
Pb(1)-Br(4)	3.125(3)		

Table S6. Pb-Br bond distances (Å) and Pb-Br-Pb angles (º) for $T_2Sn_3Br_{18}·4H_2O·0.5Br_2$.

Label	Distances	Label	Angles (°)
Sn(01)-Br(03)	2.613(6)	Br(07)-Sn(01)-Br(08)	176.4(3)
Sn(01)-Br(06)	2.630(7)	Br(07)-Sn(01)-Br(08)	178.7(3)
Sn(01)-Br(07)	2.608(7)	Br(07)-Sn(01)-Br(08)	180.0
Sn(01)-Br(08)	2.610(7)	Br(05)-Sn(02)-Br(05)#1	180.0(2)
Sn(01)-Br(0A)	2.613(6)	Br(09)-Sn(02)-Br(09)#1	180.0
Sn(01)-Br(0B)	2.586(7)		
Sn(02)-Br(04)#1	2.619(6)		

Sn(02)-Br(04)	2.619(6)
Sn(02)-Br(05)	2.610(5)
Sn(02)-Br(05)#1	2.610(5)
Sn(02)-Br(09)#1	2.592(6)
Sn(02)-Br(09)	2.592(6)

3. References

1. Sheldrick, G., SHELXT - Integrated space-group and crystal-structure determination. *Acta Crystallographica Section A* **2015,** *71* (1), 3-8.
2. Dolomanov, O. V.; Bourhis, L. J.; Gildea, R. J.; Howard, J. A. K.; Puschmann, H., OLEX2: a complete structure solution, refinement and analysis program. *Journal of Applied Crystallography* **2009,** *42* (2), 339-341.
3. Sheldrick, G., Crystal structure refinement with SHELXL. *Acta Crystallographica Section C* **2015,** *71* (1), 3-8.
4. Gate, L. F., Comparison of the Photon Diffusion Model and Kubelka-Munk Equation with the Exact Solution of the Radiative Transport Equation. *Appl. Opt.* **1974,** *13* (2), 236-238.
5. Soler, J. M.; Artacho, E.; Gale, J. D.; García, A.; Junquera, J.; Ordejón, P.; Sánchez-Portal, D., The SIESTA method forab initioorder-Nmaterials simulation. *Journal of Physics: Condensed Matter* **2002,** *14* (11), 2745-2779.
6. García, A.; Papior, N.; Akhtar, A.; Artacho, E.; Blum, V.; Bosoni, E.; Brandimarte, P.; Brandbyge, M.; Cerdá, J. I.; Corsetti, F.; Cuadrado, R.; Dikan, V.; Ferrer, J.; Gale, J.; García-Fernández, P.; García-Suárez, V. M.; García, S.; Huhs, G.; Illera, S.; Korytár, R.; Koval, P.; Lebedeva, I.; Lin, L.; López-Tarifa, P.; Mayo, S. G.; Mohr, S.; Ordejón, P.; Postnikov, A.; Pouillon, Y.; Pruneda, M.; Robles, R.; Sánchez-Portal, D.; Soler, J. M.; Ullah, R.; Yu, V. W.-z.; Junquera, J., Siesta: Recent developments and applications. *The Journal of Chemical Physics* **2020,** *152* (20), 204108.
7. Dion, M.; Rydberg, H.; Schröder, E.; Langreth, D. C.; Lundqvist, B. I., Van der Waals Density Functional for General Geometries. *Physical Review Letters* **2004,** *92* (24), 246401.
8. Cooper, V. R., Van der Waals density functional: An appropriate exchange functional. *Physical Review B* **2010,** *81* (16), 161104.
9. Cuadrado, R.; Cerdá, J. I., Fully relativistic pseudopotential formalism under an atomic orbital basis: spin–orbit splittings and magnetic anisotropies. *Journal of Physics: Condensed Matter* **2012,** *24* (8), 086005.
10. Zhang, Y.; Yang, W., Comment on ``Generalized Gradient Approximation Made Simple''. *Physical Review Letters* **1998,** *80* (4), 890-890.
11. Troullier, N.; Martins, J. L., Efficient pseudopotentials for plane-wave calculations. *Physical Review B* **1991,** *43* (3), 1993-2006.
12. Artacho, E.; Sánchez-Portal, D.; Ordejón, P.; García, A.; Soler, J. M., Linear-Scaling ab-initio Calculations for Large and Complex Systems. *physica status solidi (b)* **1999,** *215* (1), 809-817.
13. Sanchez-Portal, D.; Artacho, E.; Soler, J. M., Projection of plane-wave calculations into atomic orbitals. *Solid State Communications* **1995,** *95* (10), 685-690.